nature physics

ARTICLES

https://doi.org/10.1038/s41567-019-0471-2

Direct imaging of orbitals in quantum materials

Hasan Yavaş[1,2,5], Martin Sundermann[1,3], Kai Chen[3,6], Andrea Amorese[1,3], Andrea Severing[1,3], Hlynur Gretarsson[1,2], Maurits W. Haverkort[4] and Liu Hao Tjeng[1*]

The electronic states of quantum materials based on transition-metal, rare-earth and actinide elements are dominated by electrons in the *d* and *f* orbitals intertwined with the strong band formation of the solid. Until now, to estimate which specific orbitals contribute to the ground state and thereby determine their physical properties we have had to rely on theoretical calculations combined with spectroscopy. Here, we show that *s*-core-level non-resonant inelastic X-ray scattering can directly image the active orbital in real space, without the necessity for any modelling. The power and accuracy of this new technique is shown using the textbook example, $x^2-y^2/3z^2-r^2$ orbital of the Ni^{2+} ion in NiO single crystal.

The search for new materials with novel properties is commonly focused on materials containing transition-metal, rare-earth and/or actinide elements. The presence of the atomic-like *d* or *f* wavefunctions provide a fruitful playground to generate novel phenomena[1–5]. The intricate interplay of band formation with the local electron correlation and atomic multiplet effects leads to phases that are nearly isoenergetic, making materials' properties highly tunable by doping, temperature, pressure or magnetic field. Understanding the behaviour of the *d* and *f* electrons is essential for designing and controlling novel quantum materials. Therefore, identifying the *d* or *f* wavefunctions that actively participate in the formation of the ground state is crucial. So far, these wavefunctions have mostly been deduced from optical, X-ray and neutron spectroscopy methods in which spectra must be analysed and interpreted using theory or modelling. This, however, is also a challenge in and of itself, since ab initio calculations hit their limits due to the many-body nature of the problem. Here, we establish an experimental method that circumvents the need for involved analysis and instead provides the information as measured. With this technique, we can make a direct image of the active orbital and determine what the atomic-like object looks like in a real solid.

The spectral intensity of the dipole-allowed $s\rightarrow p$ transition depends on the orientation of the electric field polarization vector of the photon relative to the orientation of the *p* orbital[6]. Because the *s* orbital is spherically symmetric, sweeping the polarization vector over all angles yields an angular intensity distribution that directly maps the shape and orientation of the *p*-orbital hole. Yet, material research requires knowledge of the *d* and/or *f* orbital shapes. As the $s\rightarrow d$ or $s\rightarrow f$ transitions are dipole-forbidden, it has been challenging to develop an experimental method that has non-vanishing matrix elements beyond the dipole limit. However, the relatively new experimental method of non-resonant inelastic X-ray scattering (NIXS), available due to the existence of modern synchrotron facilities with high brilliance, has offered new potential.

The interaction of light with matter is given by two terms: a term proportional to the scalar product of the electron momentum operator $\mathbf{p}$ and the photon vector potential $\mathbf{A}$, and a term proportional to the vector potential $\mathbf{A}$ squared. When the photon energy matches an atomic resonance, the $\mathbf{p}\cdot\mathbf{A}$ term dominates; off-resonance, the interaction is governed by the $\mathbf{A}^2$ term. Focusing on this last term using NIXS, the double differential cross-section $\frac{d^2\sigma}{d\Omega d\omega}$ becomes proportional to the dynamical structure factor $S(\mathbf{q},\omega)$[7], which contains the material-specific information we are seeking:

$$S(\mathbf{q},\omega)=\sum_f |\langle f|e^{i\mathbf{q}\cdot\mathbf{r}}|i\rangle|^2\,\delta(\hbar\omega_i-\hbar\omega_f-\hbar\omega)$$

where $|i\rangle$ and $|f\rangle$ denote the (many-body) initial and final states, $\mathbf{q}=\mathbf{k}_i-\mathbf{k}_f$ the transferred momentum, $\hbar\omega=\hbar\omega_i-\hbar\omega_f$ the transferred energy, and $\mathbf{k}_{i,f}$ and $\hbar\omega_{i,f}$ the momentum and energy of the incoming and scattered photons, respectively.

Beyond-dipole matrix elements appear in the scattering cross-section when expanding the transition operator $e^{i\mathbf{q}\cdot\mathbf{r}}$ to the *k*th order, where *k* denotes the multipole order of the scattering cross-section[7–16]. The so-called triangular condition and parity rule restrict the number of multipoles to $|l_f-l_i|\le k\le l_f+l_i$ and $|l_i+l_f+k|=$ even for the $l_i\rightarrow l_f$ transition (respective orbital momenta of the initial and final states). This implies that for a $d\rightarrow f$ transition, only dipole ($k=1$), octopole ($k=3$) and triakontadipole ($k=5$) scattering orders occur, and for $s\rightarrow d$ (a dipole-forbidden transition) only the quadrupole transition with $k=2$ contributes to $S(\mathbf{q},\omega)$. For small momentum transfers $|\mathbf{q}|$, the NIXS spectra very much resemble dipole-allowed X-ray absorption spectroscopy (XAS). In other words, the NIXS $2p/3p\rightarrow 3d$ excitations in transition-metal compounds[8,10] or the $3d/4d\rightarrow 4f/5f$ and $5d\rightarrow 5f$ excitations in rare-earth and actinide materials[9,10] exhibit line shapes that are very similar to the ones obtained from XAS[17–21]. The only difference is that in NIXS, the direction of the momentum transfer $\hat{q}=\mathbf{q}/|\mathbf{q}|$ provides the information that is obtained from the electrical vector polarization in XAS. However, for large $|\mathbf{q}|$, for the same metal ion, the $p\rightarrow d$ or $d\rightarrow f$ transitions yield a different spectral distribution with additional features that cannot be seen in a dipole-based XAS experiment[7–16,22,23]. Moreover, the dipole-forbidden $s\rightarrow d$ or $s\rightarrow f$ transitions (quadrupolar or octopolar, respectively) now have non-vanishing matrix elements, and consequently are allowed and become visible.

Results

The novelty of our approach is to exploit these *s*-core-level transitions involving our search for a new method to determine—quantitatively

[1]Max Planck Institute for Chemical Physics of Solids, Dresden, Germany. [2]PETRA III, Deutsches Elektronen-Synchrotron (DESY), Hamburg, Germany. [3]Institute of Physics II, University of Cologne, Cologne, Germany. [4]Institute for Theoretical Physics, Heidelberg University, Heidelberg, Germany. [5]Present address: SLAC National Accelerator Lab, Menlo Park, CA, USA. [6]Present address: Helmholtz-Zentrum Berlin, BESSY II, Berlin, Germany. *e-mail: hao.tjeng@cpfs.mpg.de

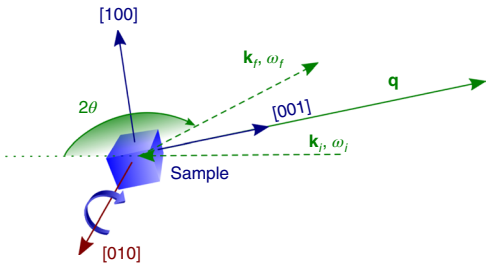

Fig. 1 | Scattering geometry of the non-resonant inelastic X-ray scattering experiment. The scattering geometry is defined by the incoming and scattered beams, $\boldsymbol{k}_i, \omega_i$ and $\boldsymbol{k}_f, \omega_f$, respectively (dashed green arrows). This geometry, which outlines the scattering triangle, remains fixed throughout the measurements. The single crystal sample (blue) is rotated around an axis perpendicular to the scattering plane (maroon) by an angle φ, and for each φ an inelastic spectrum is collected. Here, $\varphi = 0$ refers to $\mathbf{q}||[001]$ (specular geometry).

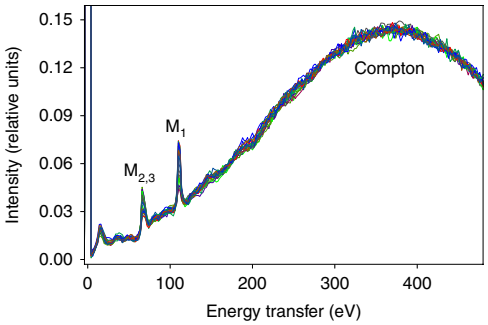

Fig. 2 | Experimental non-resonant inelastic X-ray scattering spectra of NiO containing the core level excitations on top of the Compton profile. Spectra were collected for a variety of crystal rotations φ with respect to the geometrically fixed momentum transfer vector **q**. The graph shows all the spectra. The Compton profile peaks at approximately 350 eV and is used for data normalization. The dipole-allowed Ni $M_{2,3}$ ($3p \rightarrow 3d$) edge at around 70 eV energy transfer and the dipole-forbidden Ni M_1 ($3s \rightarrow 3d$) excitations at around 110 eV can be clearly observed. The data exhibit an excellent signal-to-background (Compton) ratio in the energy range of the Ni edges, rendering NIXS a high-contrast experiment.

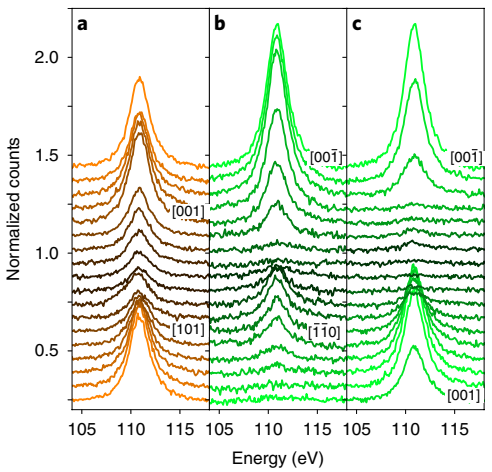

Fig. 3 | Close-up view of the experimental Ni M_1 ($3s \rightarrow 3d$) edge spectra for different sample rotations and orientations. The spectra are background-corrected and normalized. a–c, Data for momentum transfer vector **q** sweeping on a plane defined by $\mathbf{q}||[001]$ and $\mathbf{q}||[100]$ (**a**) and on a plane defined by $\mathbf{q}||[001]$ and $\mathbf{q}||[110]$ (**b**,**c**). Spectra corresponding to major axes are marked accordingly, and the spectra in between are plotted sequentially. In **b** spectra are shown where **q** is sweeping clockwise from $\mathbf{q}||[00\bar{1}]$, passing $\mathbf{q}||[\bar{1}10]$ and ending where the projection of the orbital function vanishes. Similarly, in **c**, spectra are shown where **q** is sweeping anticlockwise from $\mathbf{q}||[00\bar{1}]$ towards $\mathbf{q}||[001]$. The data are vertically shifted for clarity. The scattering intensity of the M_1 edge excitations ($3s \rightarrow 3d$) depends strongly on the relative orientation of the momentum transfer and crystallographic direction in the NiO single crystal.

and model-free—the local valence orbitals that make up the electronic structure of *d*- and *f*-containing quantum materials. We investigated the $s \rightarrow d$ transition in an inelastic X-ray scattering experiment (*s*-NIXS) at large momentum transfers $|\mathbf{q}|$ and mapped the quadrupolar scattering intensity as a function of the direction of the momentum transfer $\hat{q}$ relative to the crystal lattice. We used a single crystal of NiO (an antiferromagnetic insulator[24]) with a Ni d^8 configuration as a model system; and the large momentum transfers were guaranteed by high scattering angles and hard X-rays.

In our experimental set-up, as illustrated in Fig. 1, $S(\mathbf{q}, \omega)$ of the NiO sample was recorded as a function of the sample angle φ, here defined as the angle between the fixed momentum transfer vector **q** and the NiO surface normal (see Methods). Figure 2 shows a compilation of NIXS spectra measured for many different sample angles. The spectra show the $M_{2,3}$ edge ($3p \rightarrow 3d$) of nickel at around 70 eV and, most importantly, the dipole-forbidden M_1 ($3s \rightarrow 3d$) excitations at around 110 eV, overlaid on the broad Compton profile. The signal-to-background ratio is excellent in the energy range of the M_1 edge. A close-up of this edge and its directional dependence on **q** along $\mathbf{q}||[001]$ and $\mathbf{q}||[100]$ are displayed in Fig. 3a, and for **q** along $\mathbf{q}||[001]$ and $\mathbf{q}||[110]$ in Fig. 3b,c. In the close-up plots, the Compton profile has been subtracted using a simple linear background (see Methods).

To quantitatively analyse the $3s \rightarrow 3d$ transition's directional dependence, we determined the integrated intensity of each spectrum in Fig. 3 and placed it on a polar plot as displayed in Fig. 4. Figure 4a shows the data points for **q** sweeping in the [001]–[100] plane (orange) and Fig. 4b for **q** in the [001]–[110] plane (green). They fall accurately on top of the orbital shapes, which denote 'cuts' through the [001]–[100] (orange) and [001]–[110] (green) planes of the calculated three-dimensional (3D) orbital hole density (square of the wavefunction) of the Ni high-spin $3d^8$ configuration in octahedral coordination, namely the $^3A_2$ $3d(x^2-y^2)3d(3z^2-r^2)$ as shown in Fig. 4c. This means that we have generated a purely experimental method that can directly visualize the fundamental atomic-like quantum mechanical objects in solids. The information that we have obtained is extremely detailed; for example, we can clearly see the small lobes of the $3d(3z^2-r^2)$ contribution in Fig. 4b. We note that the $3d(x^2-y^2)$ contribution vanishes in the the [001]–[110] plane (Fig. 4b), while both $3d(x^2-y^2)$ and $3d(3z^2-r^2)$ contribute in the [001]–[100] plane (Fig. 4a). Here, we also note that we have used two orbital shapes in Fig. 4b: the blue dashed line is the $3d(x^2-y^2)3d(3z^2-r^2)$ function and the solid line is the same function convoluted with the angular acceptance of the 3×4 analysers used in the experiment (see Methods). The near perfect agreement further demonstrates the accuracy of the method, including the validity of the normalization to the Compton profile (see Fig. 5 and explanation in Methods).

Discussion

The directional dependence of the integrated *s*-NIXS intensity at the Ni M_1 edge ($3s \rightarrow 3d$) directly maps the local orbital hole density of the ion in the ground state. There is no need to carry out multiplet analysis of the spectral line shape to extract this information, in contrast to, for example, the non-*s* edges (for example, $L_{2,3}(2p)$,

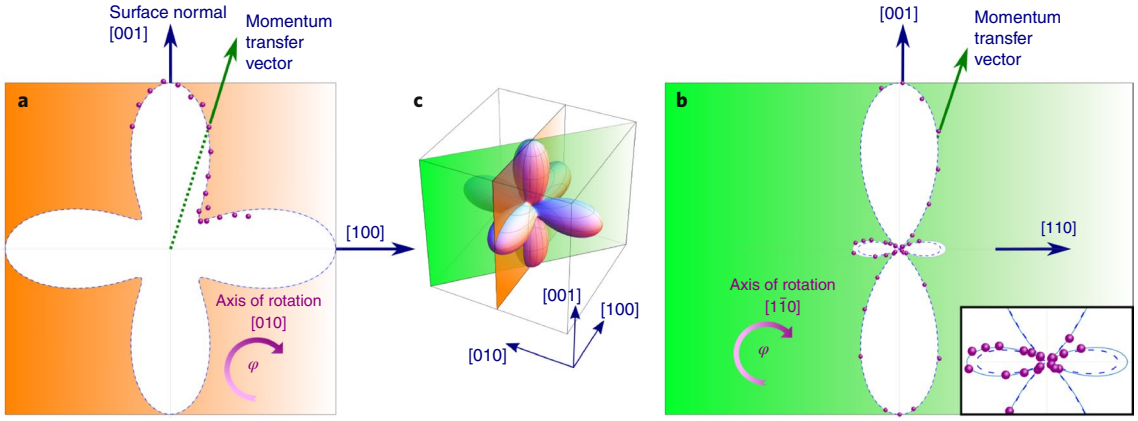

Fig. 4 | Integrated intensities of M_1 ($3s \rightarrow 3d$) edge spectra plotted on the projections of the orbital shape of the $^3A_2$ $3d(x^2-y^2)3d(3z^2-r^2)$ hole density. **a**,**b**, The projections of the 3D orbital shape on two planes are defined by [001] and [100] (**a**) and [001] and [110] (**b**). The data points on polar plots **a** and **b** are integrated intensities for Ni M_1 ($3s \rightarrow 3d$) for corresponding φ, which is the angle between the momentum transfer vector **q** and the surface normal vector [001] for both **a** and **b**. For **a** the sample is rotated such that **q** sweeps between [001] and [100]; for **b**, **q** sweeps between [001] and [110]. The inset in **b** demonstrates the theoretical orbital function (blue dashed line) and the corrected function as a result of an angular convolution with the 3×4 analyser array. For **a**, the correction was insignificant. **c**, 3D hole density distribution of the Ni high-spin $3d^8$ configuration.

$M_{2,3}$ ($3p$), $M_{4,5}$ ($3d$), $N_{4,5}$ ($4d$) and $O_{4,5}$ ($5d$)) in both NIXS[7–13,16,22,23] and XAS experiments[17–21] as well as in core-level photoemission[25]. The reason for this is fundamental: the M_1 ($3s \rightarrow 3d$) quadrupolar excitation process involves a spherically symmetric s orbital, so the angular distribution of the intensity is solely determined by the hole charge distribution in the initial state with respect to the momentum transfer **q**. This is similar to the dipole-allowed $s \rightarrow p$ transition in XAS, where an angular sweep of the polarization dependence maps out the orientation of the p hole directly. We emphasize that details of the s-NIXS final states do not matter because the information is extracted from the integrated intensity of the spectra (that is, from the sum of the intensities of all final states). As a result, only the properties of the initial state are probed. This is true for both localized and itinerant systems. This procedure of using energy-integrated spectra rather than carrying out line shape analyses has been shown to be a powerful method, for example, for determining the spin and orbital moments from X-ray magnetic dichroism experiments[26–28] and spin–orbit expectation values in inelastic X-ray scattering[14]. The power of s-NIXS, as compared to XAS, is that it allows transitions not only from s to p, but also from s to d and from s to f due to the possibility of going beyond the dipole limit when using large momentum transfers $|\mathbf{q}|$.

The s-NIXS process involves a core hole, meaning that both the electronic structure of the system and consequently the measured valence hole are projected locally. The intensity distribution is not what would be measured in an X-ray diffraction (XRD) experiment, even if such an experiment could be carried out with sufficient accuracy. In fact, it would be extremely difficult for transition-metal, rare-earth and actinide compounds to be measured with the desired accuracy in XRD due to their relatively small number of valence electrons with respect to core electrons. s-NIXS provides information complementary to that from an XRD experiment by elucidating which local orbital or atomic wavefunction is active.

The s-NIXS method presented here is not limited to ionic materials. In cases where configuration interaction effects play an important role due to covalency or itineracy, the image of the probed local orbital will reflect these effects directly. For example, in octahedral coordination one may detect e_g and t_{2g} orbital occupation ratios that are quite different from those based on the formal valency. The strength of s-core-level NIXS is that the information is extracted from the **q**-directional dependence of the integrated intensity and not from the line shape of the spectra. Thus, the details of the final states are no longer important, rendering complex configuration interaction calculations unnecessary. The sole **q**-directional dependence is rooted in the spherical symmetry of the s-core hole.

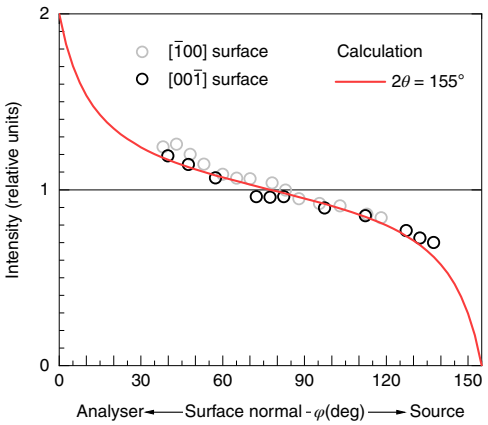

Fig. 5 | Compton intensity as function of sample angle φ. Calculated and measured Compton intensity as function of sample angle φ with respect to specular geometry ($\varphi = 77.5°$) for scattering angle $2\theta = 155°$.

The ability of s-NIXS to determine straightforwardly the local orbital is invaluable in tackling problems in complex systems where band formation and electron correlation effects are both important. This method will be able to identify, for example, the entangled spin–orbit states in ruthenium and iridium materials[29,30]. It is element-specific, and also allows for sophisticated sample environments (small samples, high pressures, high/low temperatures). New insights can be gained for a wide range of d- and f-electron-containing materials, thereby providing guidance for the design of new materials with new properties.

Online content

Any methods, additional references, Nature Research reporting summaries, source data, statements of data availability and associated accession codes are available at https://doi.org/10.1038/s41567-019-0471-2.

Received: 21 September 2018; Accepted: 13 February 2019;
Published online: 25 March 2019

References

1. Cava, R. J. Oxide superconductors. *J. Am. Ceram. Soc.* **83**, 5–28 (2008).
2. Khomskii, D. I. *Transition Metal Compounds* (Cambridge Univ. Press, 2014).
3. Keimer, B., Kivelson, S. A., Norman, M. R., Uchida, S. & Zaanen, J. From quantum matter to high-temperature superconductivity in copper oxides. *Nature* **518**, 179–186 (2015).
4. Wirth, S. & Steglich, F. Exploring heavy fermions from macroscopic to microscopic length scales. *Nat. Rev. Mater.* **1**, 16066 (2016).
5. Pfleiderer, C. Superconducting phases of *f*-electron compounds. *Rev. Mod. Phys.* **81**, 1551–1624 (2009).
6. Fowles, G. R. *Introduction to Modern Optics* (Holt, Rinehart and Winston, 1968).
7. Schülke, W. *Electron Dynamics by Inelastic X-ray Scattering* (Oxford Univ. Press, 2008).
8. Haverkort, M. W., Tanaka, A., Tjeng, L. H. & Sawatzky, G. A. Nonresonant inelastic X-ray scattering involving excitonic excitations: the examples of NiO and CoO. *Phys. Rev. Lett.* **99**, 257401 (2007).
9. Gordon, R. A. et al. High multipole transitions in NICS: valence and hybridization in 4*f* systems. *Europhys. Lett.* **81**, 26004 (2008).
10. Gordon, R. A., Haverkort, M. W., SenGupta, S. & Sawatzky, G. A. Orientation-dependent X-ray Raman scattering from cubic crystals: natural linear dichroism in MnO and CeO_2. *J. Phys. Conf. Ser.* **190**, 012047 (2009).
11. Bradley, J. A. et al. Probing electronic correlations in actinide materials using multipolar transitions. *Phys. Rev. B* **81**, 193104 (2010).
12. Caciuffo, R. et al. Uranium 5*d*–5*f* electric-multipole transitions probed by nonresonant inelastic X-ray scattering. *Phys. Rev. B* **81**, 195104 (2010).
13. Bradley, J. A., Moore, K. T., van der Laan, G., Bradley, J. P. & Gordon, R. A. Core and shallow-core *d*- to *f*-shell excitations in rare-earth metals. *Phys. Rev. B* **84**, 205105 (2011).
14. van der Laan, G. Spin–orbit sum rule for electric multipole transitions in nonresonant inelastic X-ray scattering. *Phys. Rev. Lett.* **108**, 077401 (2012).
15. van der Laan, G. Nonresonant inelastic X-ray scattering from actinides and rare earths. *Phys. Rev. B* **86**, 035138 (2012).
16. Willers, T. et al. Determining the in-plane orientation of the ground-state orbital of $CeCu_2Si_2$. *Phys. Rev. Lett.* **109**, 046401 (2012).
17. Chen, C. T. et al. Out-of-plane orbital characters of intrinsic and doped holes in $La_{2-x}Sr_xCuO_4$. *Phys. Rev. Lett.* **68**, 2543–2546 (1992).
18. de Groot, F. X-ray absorption and dichroism of transition metals and their compounds. *J. Electron Spectros.* **67**, 529–622 (1994).
19. Tanaka, A. & Jo, T. Resonant 3*d*, 3*p* and 3*s* photoemission in transition metal oxides predicted at 2*p* threshold. *J. Phys. Soc. Jpn* **63**, 2788–2807 (1994).
20. Csiszar, S. I. et al. Controlling orbital moment and spin orientation in CoO layers by strain. *Phys. Rev. Lett.* **95**, 187205 (2005).
21. Hansmann, P. et al. Determining the crystal-field ground state in rare earth heavy fermion materials using soft-X-ray absorption spectroscopy. *Phys. Rev. Lett.* **100**, 066405 (2008).
22. Sundermann, M. et al. Direct bulk-sensitive probe of 5*f* symmetry in URu_2Si_2. *Proc. Natl Acad. Sci. USA* **113**, 13989–13994 (2016).
23. Sundermann, M. et al. 4*f* crystal field ground state of the strongly correlated topological insulator SmB_6. *Phys. Rev. Lett.* **120**, 016402 (2018).
24. Sawatzky, G. A. & Allen, J. W. Magnitude and origin of the band gap in NiO. *Phys. Rev. Lett.* **53**, 2339–2342 (1984).
25. Hamamoto, S. et al. Linear dichroism in angle-resolved core-level photoemission spectra reflecting 4*f* ground-state symmetry of strongly correlated cubic Pr compounds. *J. Phys. Soc. Jpn* **86**, 123703 (2017).
26. Thole, B. T., Carra, P., Sette, F. & van der Laan, G. X-ray circular dichroism as a probe of orbital magnetization. *Phys. Rev. Lett.* **68**, 1943–1946 (1992).
27. Carra, P., Thole, B. T., Altarelli, M. & Wang, X. X-ray circular dichroism and local magnetic fields. *Phys. Rev. Lett.* **70**, 694–697 (1993).
28. Chen, C. T. et al. Experimental confirmation of the X-ray magnetic circular dichroism sum rules for iron and cobalt. *Phys. Rev. Lett.* **75**, 152–155 (1995).
29. Jackeli, G. & Khaliullin, G. Mott insulators in the strong spin–orbit coupling limit: from Heisenberg to a quantum compass and Kitaev models. *Phys. Rev. Lett.* **102**, 017205 (2009).
30. Jain, A. et al. Higgs mode and its decay in a two-dimensional antiferromagnet. *Nat. Phys.* **13**, 633–637 (2017).

Acknowledgements

M.S., K.C. and A.S. acknowledge support from the German funding agency DFG under grant no. SE1441-4-1.

Author contributions

L.H.T. and M.W.H. initiated the project. H.Y., M.S., K.C., A.A. and H.G. performed the experiment and analysed the data. H.Y., A.S., M.W.H. and L.H.T. wrote the manuscript with input from all authors.

Competing interests

The authors declare no competing interests.

Additional information

Reprints and permissions information is available at www.nature.com/reprints.

Correspondence and requests for materials should be addressed to L.H.T.

Publisher's note: Springer Nature remains neutral with regard to jurisdictional claims in published maps and institutional affiliations.

Methods

Experiment. NIXS measurements were performed at the High-Resolution Dynamics Beamline P01 of PETRA-III synchrotron in Hamburg, Germany. Figure 1 illustrates the experimental set-up, showing the incoming beam $(\mathbf{k}_i, \omega_i)$, sample, scattered beam $(\mathbf{k}_f, \omega_f)$ and the corresponding momentum transfer vector $(\mathbf{q})$. The energy of the X-ray photon beam incident on the sample was tuned with a Si(311) double-reflection crystal monochromator (DCM). The photons scattered from the sample were collected and energy-analysed by an array of 12 spherically bent Si(660) crystal analysers. The analysers are arranged in a 3×4 configuration. The energy of the analysers ($\hbar\omega_f$) was fixed at 9,690 eV, and the energy loss spectra were measured by scanning the energy of the DCM ($\hbar\omega_i$). Each analyser signal was individually recorded by a position-sensitive custom-made LAMBDA detector. The energy calibration was regularly checked by measuring the zero-energy-loss position of each spectrum. The best possible energy resolution was guaranteed by pixel-wise analysis of the detector recordings and measured as 0.7 eV (full-width at half-maximum).

The positioning of the analyser array determines the momentum transfer vector and the corresponding scattering triangle, which is defined by the incident and scattered photon momentum vectors, $\mathbf{k}_i$ and $\mathbf{k}_f$, respectively. The large scattering angle ($2\theta \approx 155°$) chosen for the current study assured a large momentum transfer of $|\mathbf{q}| = (9.6 \pm 0.1)\,\text{Å}^{-1}$ when averaged over all analysers. $\mathbf{k}_f$ and 2θ were kept constant by fixing the energy and the position of the analyser array. Because the energy transfer range of interest (100–120 eV) was small with respect to the incident and final energies (~9,700 eV), variation of $\mathbf{k}_i$ during energy scanning was insignificant. This guaranteed that the scattering triangle was virtually unchanged throughout the course of the experiment with $|\mathbf{q}| \approx$ constant.

Sample. NiO single crystal (SurfaceNet) was kept at 20 K throughout the experiment. It was aligned as in Fig. 1 and rotated by angle φ around an axis perpendicular to the [010] lattice direction; $\mathbf{q}||[001]$ ($\varphi = 0$) corresponds to specular geometry. Energy scans were taken for many values of φ so that the directional dependence of $S(\mathbf{q}, \omega)$ could be measured for $\mathbf{q}$ sweeping between $\mathbf{q}||[001]$ and $\mathbf{q}||[100]$. For the second set of measurements, the crystal was reoriented to evaluate $S(\mathbf{q}, \omega)$ on $\mathbf{q}||[001] - \mathbf{q}||[100]$. This time, the axis of rotation was along $[1\bar{1}0]$. Each φ data point took about 90 min, in which the elastic peak, Compton profile and the *s*-NIXS edge were recorded. The data collection for the NiO project took about 3 days.

Data treatment. The data were normalized to the Compton peak at about 350 eV energy transfer (Fig. 2). Subsequently, a linear background was subtracted from each spectrum to account for the Compton scattering in the energy range of the Ni M_1 edge.

We note that the line shape of the Compton profile does not change with angle as can be seen in Fig. 2. This is fully consistent with the fact that the scattering geometry is kept constant while rotating the sample. What does vary is the intensity of the Compton scattering. This is related to how the X-rays are absorbed when entering the sample and when scattered out of the sample. This process can be modelled quantitatively because the NiO crystals used have well-defined (flat and shiny) surfaces. The result of this modelling and the comparison with the experiment is displayed in Fig. 5. The calculations were done for the actual scattering geometry of $2\theta = 155°$ so that for $\varphi = 77.5°$ specular geometry is fulfilled. Turning the sample towards (away from) the analyser increases (decreases) the intensity. One can observe a very good overall match between the experiment and the modelling. Slight deviations on the order of a few percent can be ascribed to imperfections in the kapton-glue-aluminium windows (that is, from variations in thickness) of our cryostat. Figure 5 therefore demonstrates that we understand fully the details of the scattering process, and in particular, that the intensity variations of the Compton profile are due to the absorption processes in the sample (and also in the cryostat windows). We can therefore safely use the Compton profile to normalize our *s*-NIXS spectra.

Because the analyser array (3×4) is spread over a finite solid angle, each measured spectrum $S(\mathbf{q}, \omega)$ includes an array of momentum transfer vectors $\mathbf{q}$ corresponding to individual analysers. In this case, taking an average $\mathbf{q}$ does not work for directions where the orbital wavefunction varies significantly for small angular changes (that is, small lobes of $3d(3z^2 - r^2)$). The theoretical orbital wavefunction should be convoluted with the angular spread of the analyser array to reflect this effect. The inset of Fig. 4b demonstrates the theoretical function (blue dashed line) and the convoluted function (solid line), which agrees well with the data points.

Data availability

The data that support the findings of this study are available from the corresponding authors upon request.